Experimental tests and numerical simulation of delamination and fiber breakage in AP-PLY composite laminates

Zheng, Weiling; Kassapoglou, Christos

DOI
10.1177/07316844241245469

Publication date
2024

Document Version
Final published version

Published in
Journal of Reinforced Plastics and Composites

JOURNAL OF REINFORCED PLASTICS & COMPOSITES

Original Article

Journal of Reinforced Plastics and Composites
2024, Vol. 0(0) 1–13

DOI: 10.1177/07316844241245469
journals.sagepub.com/home/jrp
Sage

Experimental tests and numerical simulation of delamination and fiber breakage in AP-PLY composite laminates

Weiling Zheng[1] and Christos Kassapoglou[2]

Abstract

The behavior of delaminations and fiber breakage resulting from three-point bending test is a major concern in the study of composites. This research focused on analyzing fiber breakage and delaminations in advanced placed ply composite laminates through a series of tests. In order to compare simulation results with the experimental data, the cohesive zone model was implemented for analyzing the damage in the model. The results of the simulation were validated using experimental results. The predicted damage initiation load exhibited an approximate 20% deviation from the actual test loads and the discrepancy stems are analyzed.

Keywords

Fabrics/textiles, delamination, fracture, mechanical testing

Introduction

Composite laminates are widely utilized in the aerospace industry due to their excellent damage tolerance, high stiffness and strength, low density, and adaptability for specific applications. However, the weak interlaminar strength in the transverse direction makes composites susceptible to delamination under out-of-plane loads. Delamination can originate from manufacturing defects, matrix cracks, fiber breaks, or out-of-plane loads, and it is a common damage mode in composite laminates. Fiber breakage is another damage mode which, eventually, is responsible for final failure of the structure. When present, these two types of damage reduce the overall stiffness of a laminate. More importantly, if they grow sufficiently, they may lead to laminate failure.

In the past decades, researchers have developed various methods to investigate composite damage and many focused on the determination of delamination onset. Existing approaches for determining delamination onset are based on stress[1–4] and fracture mechanics.[5–8]

Delamination propagation studies in composite laminates often utilize fracture mechanics, wherein parameters such as the strain energy release rate (SERR), and stress intensity factors are needed. According to fracture mechanics, delamination propagation can be determined by comparing the strain energy release rate G at the crack tip with the critical energy release rate G_c.

In comparison to conventional composite laminates, advanced placed ply (AP-PLY) composites have gained attention from researchers and industry professionals due to their improved tailorability and higher damage tolerance.[9,10] The mechanical properties of AP-PLY composite laminates are predicted using laminate theory, finite element analysis, and experimental methods.

Laminate theory assumes that the woven unit structure in AP-PLY comprises multiple unidirectional laminates with equal fiber volume fractions. The global stiffness matrix is constructed by assembling a single stiffness matrix for each individual laminate. Whitney and Chou[11] analyzed the geometric configuration of three-dimensional woven composites based on the concept of micro-cells. Ishikawa and Chou[12] proposed three one-dimensional models: Mosaic Model, one-dimensional Fiber Undulation Model, and Bridging Model, and they obtained the average in-plane elastic constants of woven composites by averaging the results from all three models using classical laminate theory. Naik and Kuchibhotla[13] proposed a two-dimensional analytical method for the failure behavior of plain weave fabric

[1]School of Power and Energy, Northwestern Polytechnical University, Xi'an, China
[2]Department of Aerospace Structures and Materials, Delft University of Technology, Delft, Netherlands

Corresponding author:
Weiling Zheng, School of Power and Energy, Northwestern Polytechnical University, 127 West Youyi Road, Beilin District, Xi'an, Shaanxi 710072, China. Emails: w.zheng@nwpu.edu.cn; zhwl_0130@163.com

Data Availability Statement included at the end of the article.

composites made of twisted yarns under tensile loading and the cross-section area of the yarn was taken to be elliptical and the yarn path was taken to be sinusoidal. Sankar and Marrey[14] introduced a selective averaging method for predicting the elastic modulus of two-dimensional (2D) plain woven composites, which involves averaging the stiffness and compliance values.

In addition to adopting laminate theory, the finite element method has gained popularity among scientists due to advancements in computer science. Woo and Whitcomb[15] utilized macro-scale elements in the global/local finite element model to analyze the stress distribution within woven composites. Tan[16] considered elliptical cross-sections of yarns and an isotropic stiffness matrix, while assuming that the warp, weft, and Z yarns are orthogonal to the material spindles after resin saturation. Chen[17] proposed a finite multiphase element method to predict the effective elastic properties of three-dimensional (3D) braided composites based on the variational principle and different unit cell assumptions for the interior, surface, and corner regions in the 3D braided composites. Byun and Chou[18] developed a model based on the fabric geometry to predict the thread volume fractions and elastic constants of 3D angle-interlock fabric composites. Madenci et al.[19] investigated the flexture performances of pultruded glass FRP composite beams using experimental method, finite element method, and theoretical method.

The mechanical properties of woven composites have been investigated through testing. Zhao et al.[20] observed the effect of tackification on the in-plane shear behavior of biaxial woven fabric through a bias extension test. Gemi et al.[21] evaluated the damage of low velocity impact of filament wound composite pipes experimentally and statistically. Cai et al.[22] compared the failure of plain woven glass/epoxy laminates under off-axis and biaxial tension loadings. Zheng and Kassapoglou[23,24] employed the finite element method to predict the delamination onset and propagation of AP-PLY composite laminates and later proposed an energy method based on beam theory to determine the stress intensity factor and analyze the delamination growth of existing cracks in composite beams. This included a procedure to obtain the stress intensity factor of a crack growing in regions of variable stiffness, with the analytical stress intensity factor used for the optimization of AP-PLY composite laminates,[25] neglecting geometric discontinuities of the tows in the models. Li et al.[26] introduced a tow-wise modeling approach to explicitly depict gaps/overlaps, tow drops, and out-of-plane waviness, and the capability of this approach was validated in predicting the failure mechanisms of AP-PLY laminates in a short beam shear test.[27]

The present study investigated the delamination behavior of AP-PLY composite laminates under out-of-plane loads. Specifically, the focus was on the mode II delamination test, where the composite laminate is woven in only one direction. The paper includes details about specimen preparation, experimental setup, measurement technique, and experimental procedure. The chosen specimen configuration is a special case of AP-PLY that avoids the interaction of the weaving pattern in one direction with that in another. The test results are then analyzed and compared with simulation results.

Material and methods

Materials and specimen preparation

To simplify the configuration and improve our understanding, this paper considers AP-PLY composite laminates woven in only one direction. Although the manufacturing process is similar to plain woven AP-PLY, there are modifications in the second and fourth steps to ensure that the produced AP-PLY is woven in one direction, as shown in Figure 1. A particular characteristic of the structure of an AP-PLY laminate is that it has interwoven layers delineated by woven plies and the straight plies in the other direction used to fill the space created by the woven layers. In the structure, the green plies (dark color) are the straight plies that are used to fill the gap left by the woven ply. The width of space between the filled plies is the same as the width of the ply. Taking into account the fact that AP-PLY structures are made using fiber placement, a width of 6.35 mm was chosen as the tow width used in the architecture with a thickness of 0.18 mm.

For the experiments, a 24-layer AP-PLY composite laminate was manufactured using carbon fiber AS4 and epoxy resin 8552. The matrix material has the material properties: Young's modulus E = 4.56GPa and Poisson's ratio $\vartheta = 0.3$. The material properties used for the model were the same as those of HexPly AS4/8552, as shown in Table 1. Note that the values for E_3, G_{23} and ϑ_{23} are assumed estimates. The subscripts 1, 2, and 3 are used to denote direction parallel to the fibers, transverse, and thickness direction, respectively. The geometry of the manufactured AP-PLY composite laminate is as follows: length $L_1 = 202mm$, width $L_2 = 191.5mm$, thickness $t = 4.59mm$, as shown in Figure 2. The lay-up sequence is $[90_5/0_5/(0^w/90^f)/90/0/0_5/90_5]$, where the 0° ply is woven with the 90° ply using a woven pattern in one direction. The superscripts of "w" denotes the woven ply in the stacking sequence and "f" denotes the filled ply in the lay-up sequence from top to bottom in the z direction. The fabricated laminate was cured in an autoclave according to the material manufacturer's specifications.

The AP-PLY composite laminate was sectioned into smaller specimens using a STRUERS Secotom-10 cutting machine with a specially designed diamond blade for carbon fiber-reinforced composite laminates, utilizing the water jet cutting process.

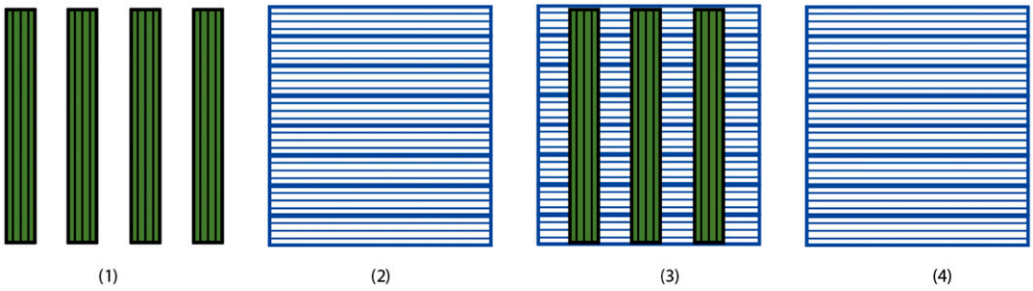

Figure 1. Manufacturing of AP-PLY woven in one direction.

Table 1. Ply's material properties.

Young's modulus	Shear modulus	Poisson's ratio
$E_1 = 148GPa$	$G_{12} = 4.55GPa$	$\vartheta_{12} = 0.3$
$E_2 = 9.65GPa$	$G_{13} = 4.55GPa$	$\vartheta_{13} = 0.3$
$E_3 = 9.65GPa$	$G_{23} = 3.64GPa$	$\vartheta_{23} = 0.45$

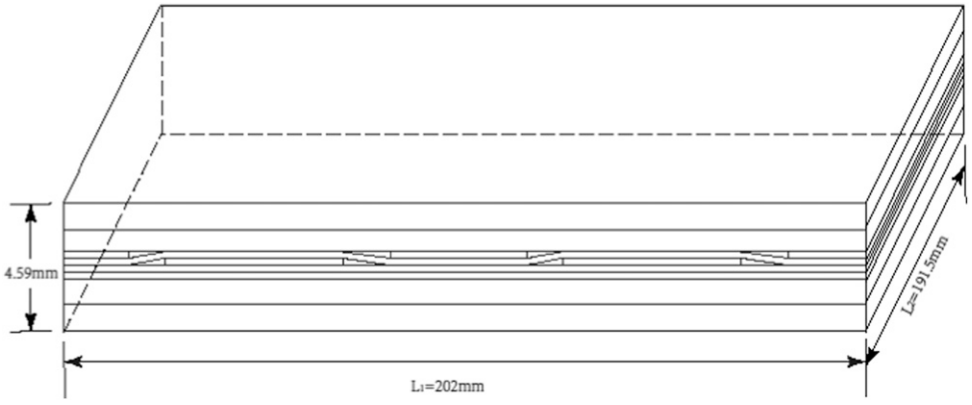

Figure 2. Geometry of AP-PLY composite laminate.

The first two tests were conducted on 24-layer specimens of the AP-PLY composite laminate. The remaining seven tests utilized 14-layer specimens, which were created by removing the top five layers and bottom five layers from the 24-layer laminate. This modification was based on the results of the initial tests, where the top and bottom 90_5 plies experienced early transverse tension or compression failures. The top layers failed due to cracking caused by crushing loads on the loading tab, while the bottom layers failed due to transverse tension. A DECKEL cutting machine was used to remove the five top layers and five bottom layers. It should be noted that due to the non-straight or non-flat nature of the plies, it was not possible to completely remove all five top layers and five bottom layers. As a result, thin patches of 90° fibers remained on some specimen surfaces. Refer to Figure 3 for a depiction of a surface after the removal of top and bottom layers.

During the experiment, strain gauges (KFG-5-120-C1-23) from KYOWA with a gauge factor of 2.12 + 1.0% were utilized to measure strain on the top and bottom surfaces of a coupon. Two strain gauges were placed at $\frac{1}{4}L$ and $\frac{3}{4}L$ on the top surface, while three were placed at $\frac{1}{4}L, \frac{1}{2}L$ and $\frac{3}{4}L$ on the bottom surface in the longitudinal direction (see Figure 4).

The edges of the specimens were painted flat white to visually inspect for any signs of delamination using the naked eye or a high-resolution digital camera. The highlighted surface in Figure 5 illustrates the woven structure of the AP-PLY.

Any moisture absorbed during previous operations, specifically water jet cutting, was removed by placing the painted coupon in an oven set at a temperature of 60℃ for 72 h. Before and after being placed in the oven, each of the four specimens was weighed. The weights are listed in

Table 2, where wm1 represents the weight before being placed in the oven, wm2 represents the weight after being taken out of the oven, δwm is the weight difference (wm1 − wm2), and ratio is the percentage change in weight $\left(\frac{\delta wm}{wm2}\right)$. The specimen used in test 1 consisted of 24 layers and was significantly heavier than the other three specimens used in tests 7, 8, and 9. Additionally, the specimens in tests 7, 8, and 9 had slightly different weights due to variations in specimen width. The average moisture uptake ratio across all specimens was 0.116%, with δwm as the standard deviation.

Test

During testing, a pilot experiment was initially conducted due to the lack of a standardized testing method for mode II delamination of AP-PLY composite laminates. It was uncertain whether delamination occurred before fiber breakage or before transverse cracks developed in the matrix. The weaving pattern was also expected to have a significant impact on delamination onset and growth. Therefore, the specimen preparation process was carried out step by step and repeated based on the results of previous tests, with adjustments made as necessary. The tests included mechanical testing and evaluation of the specimen surfaces under a microscope.

Mechanical testing provided material properties necessary for understanding the physical behavior of the composite laminate. These properties served as inputs in finite element analysis and numerical simulations. In this study, three-point bending tests were carried out. Due to the complexity of the AP-PLY structure, it was challenging to follow the specimen dimension guidelines because the AP-PLY pattern interfered with loading tabs or would not be at the desired location and to meet the requirements of existing standards for three-point bending tests shown in Figure 6 (ASTM standard 7264).

The experimental setup consisted of a span length L of 50.4mm and two support steel rods with diameters d_1 of 30mm. The specimen length L_0 slightly differed from L, and the loading nose diameter d_2 (which will be described later) ensured symmetry in the x direction with respect to the loading point. Since there was no specific standard adopted for the test, two adjustable parameters were considered: the diameter of the loading nose and the number of silicone pads used between the loading nose and the specimen.

To account for these parameters, two different sizes of loading nose with diameters d_2 of 15mm and 25mm were used. Additionally, three variations of the silicone pad were tested: (1) no silicone pad, (2) one-layer silicone pad (thickness t of 0.54mm), and (3) two-layer silicone pad. It should be noted that the silicone pads were placed directly underneath the loading nose.

The experimental setup for the three-point bending test is illustrated in Figure 7. The loading nose was positioned equidistant from the steel rod supports and perpendicular to the specimen. If the loading nose exceeded the width of the specimen, the specimen was centered with respect to the loading nose. Throughout the test, the positions of the specimen and steel rod supports remained fixed.

To monitor the behavior of the specimen during loading, two high-resolution digital cameras connected to a computer automatically recorded images of both the front and back surfaces of the specimen at one-second intervals. Load and displacement data were transferred to a computer and stored in an Excel file, facilitating data analysis after the test. The woven surface of the specimen during testing could be observed on a monitor through the two cameras depicted in Figure 6. All three-point bending tests were conducted using a 10 kN tensile and compression Zwick machine.

The primary objective of the tests was to investigate the delamination behavior of AP-PLY composite structures

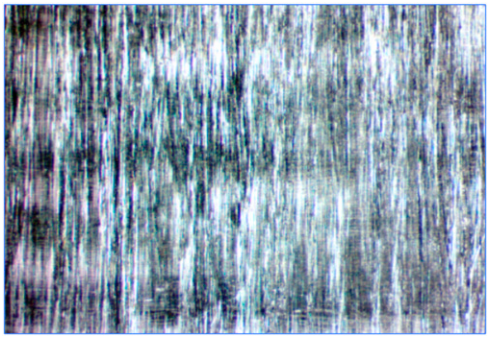

Figure 3. Surface after removing the five outermost layers (photo taken looking down on the specimen).

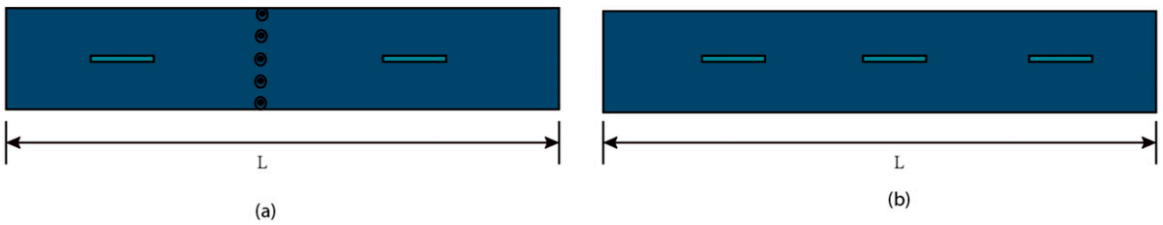

Figure 4. Strain locations for the AP-PLY specimen: (a) top surface and (b) bottom surface.

under various loads. Therefore, it was crucial to carefully monitor and observe any delamination occurrence during the testing process. Delamination detection was carried out using visual inspection, as well as by analyzing the images captured by the cameras and displayed on the monitor. The tests were performed with displacement control, using a fixed displacement rate of 0.5 mm/min.

In composite laminates, the resin pockets that are present are susceptible to delamination initiation due to their relatively weaker and less stiff properties compared to the fibers. To gain insight into the expected behavior of the specimens, a 2D AP-PLY composite laminate finite element beam model, based on our previous work,[23] was developed. The finite element model was linear when the deflection was low during the initial crack and delamination stages. The predicted load for delamination initiation in the linear stage of the 2D AP-PLY model, obtained from the finite element analysis, was used as the anticipated load for the test. The predicted delamination initiation load for a 3D composite beam can be calculated as $F_{ini} = b \times P_{pre}$, where b is the width of the 3D composite beam, and P_{pre} is the predicted onset of delamination load per specimen width from the 2D finite element beam model.

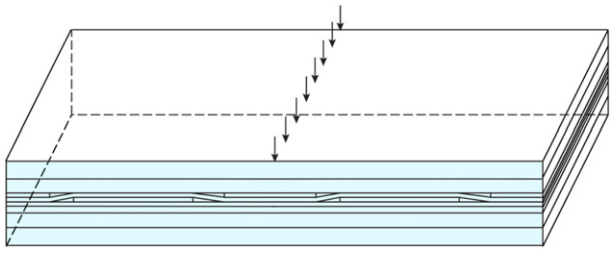

Figure 5. Specimen with painted surface highlighted.

Table 2. Weights of different specimens.

Name	Test 1	Test 7	Test 8	Test 9
wm1	12603.5mg	8328.9mg	7804.1 mg	8893.4 mg
wm2	12587.2mg	8321.3mg	7795.9 mg	8881.3 mg
δwm	16.3mg	7.6mg	8.2 mg	12.1 mg
ratio	0.1295%	0.0913%	0.1052%	0.1362%

Different loading procedures were employed for the 24-layer and 14-layer specimens. For the 24-layer specimens, the procedure was as follows: a linear load was applied, gradually increasing from zero to the anticipated delamination initiation load at a rate of 0.5mm/ min. Once the expected initiation load was reached, the load was held constant for 1 min. Subsequently, the load was increased by $0.05F_{ini}$ and held for 1 min. This process was repeated until the load reached $1.75F_{ini}$. If no damage was observed, the load was increased in 300N increments, with 1-min intervals, until reaching 6300N. The test then continued monotonically until a load of 10,000 N was reached, at which point the test was concluded.

For the 14-layer specimens, the loading procedure had the same displacement rate, but the applied load increased from 0 to 2500 N and was held for 20 s. Subsequently, the load was increased in 250 N increments until reaching 3500 N. After that, the load was increased by 100 N in each step until reaching 7000 N. The load was then increased monotonically up to 10,000 N, at which point the test was

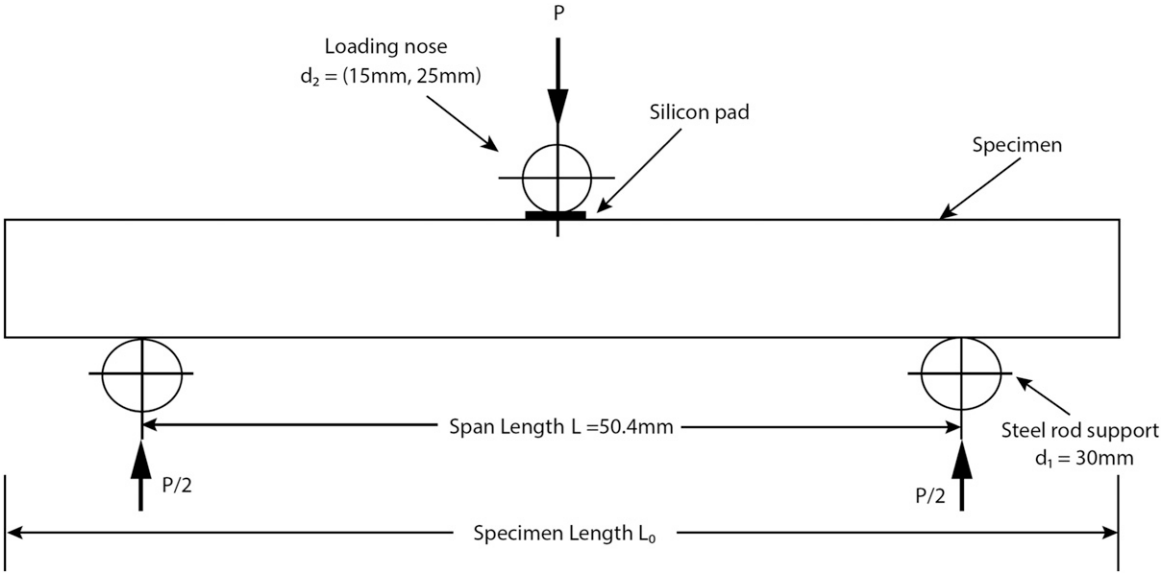

Figure 6. Three-point bending diagram.

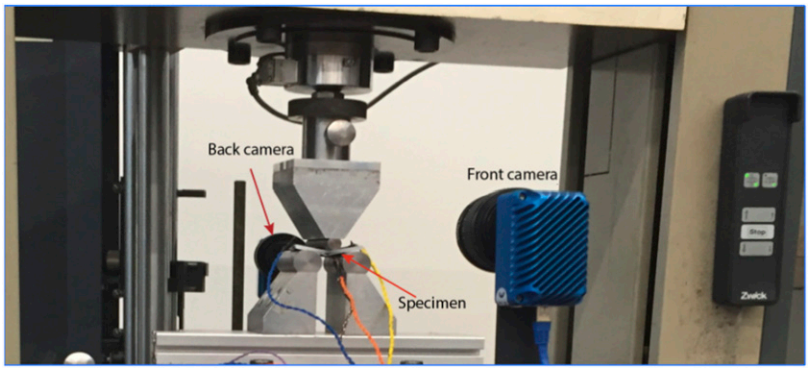

Figure 7. Three-point bending test setup.

terminated. It is important to note that the test was halted if any audible signs of damage were detected. Figure 8 provides an example of the loading procedure used in test 7.

Microscopy was employed to examine the fracture behavior of the specimen subsequent to the mechanical test. Two types of microscopes were utilized for observing the painted surfaces following the 3PB test. The first microscope employed was the ZEISS AxioCam ERc5S camera, capable of a maximum magnification of 8x, allowing for direct observation of the deformed structure's surface or, post-test, to inspect the polished surface. In order to achieve a polished surface, 400 grit sandpaper first and later 1000 grit sandpaper were utilized. The second microscope utilized was the Leica DM LM system, an optical microscope with a maximum magnification of 100x. The observed samples were mounted and embedded in a green epoxy compound to ensure that the cross-section was flat within the embedded material. The embedded samples, depicted in Figure 9, were prepared for optical microscopy following the process of curing, grinding, and polishing.

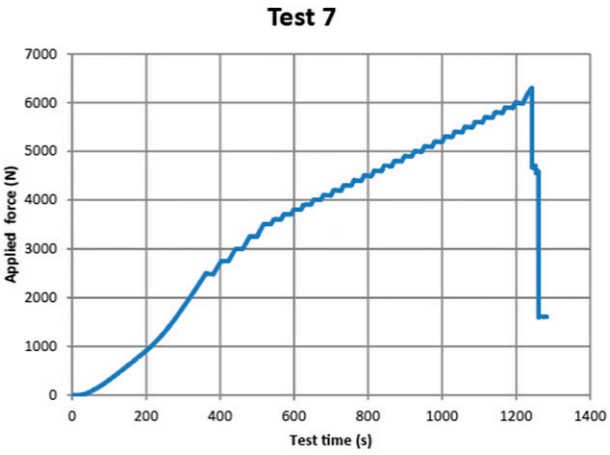

Figure 8. Loading procedure in test 7.

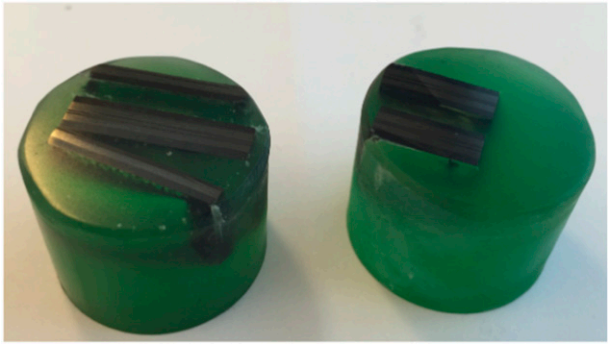

Figure 9. Embedded tested samples.

Results

Test results of the 24-layer specimens

The aim of the tests was to evaluate delamination in AP-PLY composite laminates subjected to three-point bending. The first two tests involved 24-layer AP-PLY composite specimens, utilizing a loading block with $d_2 = 15mm$, and no silicone pad between the loading rod and the specimen. The first test was terminated upon the detection of a noise, while the second test ended upon reaching complete failure, indicated by a 50% drop in load. Both tests showed crack initiation at the center of the bottom surface, where the tensile stress due to the moment was highest. Refer to Figure 10 for visual representation of the damage.

Each specimen was fitted with five strain gauges, with a gauge limit of 1%. Figure 11 presents the strains experienced at the $\frac{1}{4}L$ and $\frac{3}{4}L$ positions on the top surface, as well as the strains observed at the $\frac{1}{4}L$, $\frac{1}{2}L$ and $\frac{3}{4}L$ locations on the bottom surface throughout the test. The maximum strain occurred at the central point $\frac{1}{2}L$. Due to the structural symmetry at the load point, the strain at $\frac{1}{4}L$ matched that at $\frac{1}{4}L$. Additionally, the strain at $\frac{1}{4}L$ on the top surface displayed a different sign but nearly identical magnitude to the strain at the corresponding position on the bottom surface. This is

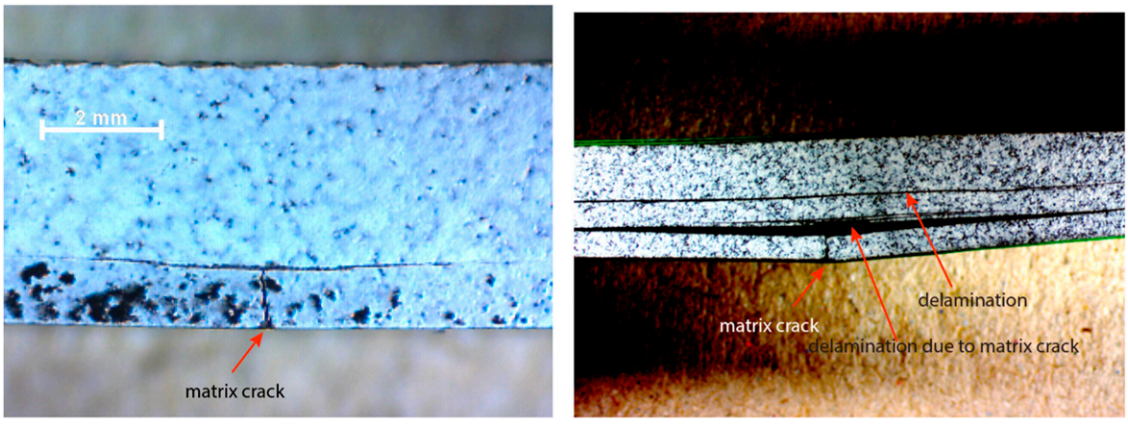

Figure 10. Damage of specimens after testing: (a) specimen 1 embedded tested sample and (b) specimen 2.

attributed to the compression on the top surface and tension on the bottom surface, aligning with our expectations.

Considering the slight discrepancies in specimen widths, the crack initiation load was normalized with respect to the width, denoted as $F_b = \frac{F}{b}$, where F represents the crack initiation load in the test and b denotes the width of the specimen. Test 1 yielded F_b value of 47.93N/mm, while test 2 resulted in F_b value of 49.435N/mm. Furthermore, it was observed that the transverse matrix crack initiated at the bottom surface instead of delamination at the interface of different layers, mainly due to the 90_5 lay-up of the top and bottom layers.

Naked eye examination did not allow for the detection of damage beyond broken fibers and delamination caused by the transverse crack reaching the 90/0 ply interface. Therefore, the specimens were cut into four equal pieces for further investigation. The cut pieces were initially examined using the ZEISS microscope. Due to its lower magnification and the presence of an unpolished rough surface, it was challenging to discern whether resin areas contained cracks. Subsequently, the embedded smaller pieces were examined via optical microscopy, as presented in Figure 12.

Analysis revealed that delamination in specimen 1 resulted from the transverse failure of the matrix in the bottom five layers, which were 90_5 plies, as illustrated in Figure 10. Specimen 2, however, displayed an additional delamination not due to matrix failure, following the transverse matrix failure of the bottom five layers. To mitigate the occurrence of transverse failure in the 90 plies, the top five layers of 90_5 and the bottom five layers of 90_5 were removed in the remaining specimens, resulting in 14-layer AP-PLY composite laminate specimens with a nominal thickness of 2.52mm.

Test results of the 14-layer specimens

In the remaining seven tests, the specimens consisted of 14 layers, two of which had an AP-PLY pattern. In test 3, the

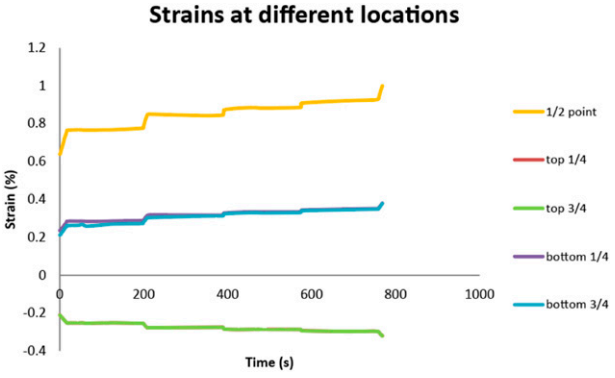

Figure 11. Strains at different locations of the specimen.

displacement exceeded the specimen's thickness when damage occurred, and the strains measured exceeded the strain gauges' range. Consequently, strain gauges were no longer used in the subsequent tests. The specimen structures in tests 3 and 4, referred to as structure A, were identical to the one shown in Figure 5. The structure of specimens used in tests 5, 7, 8, and 9, referred to as structure B, is presented in Figure 13(a), while the structure of the specimen used in test 6, referred to as structure C, is shown in Figure 13(b). Structure B is the mirrored version of structure A, while structure C is a specimen cut from another location where structural symmetry is maintained.

Similarly to earlier tests, two parameters were considered in the remaining seven tests: the diameter of the loading nose and the number of silicone pads used between the loading nose and specimens. The test parameters, damage initiation loads, and locations are provided in Table 3. For example, in test 3, the diameter of the loading nose was 15mm, and no silicone pads were used. The damage initiated from the top layer, and the initiation load was 115.2N/mm.

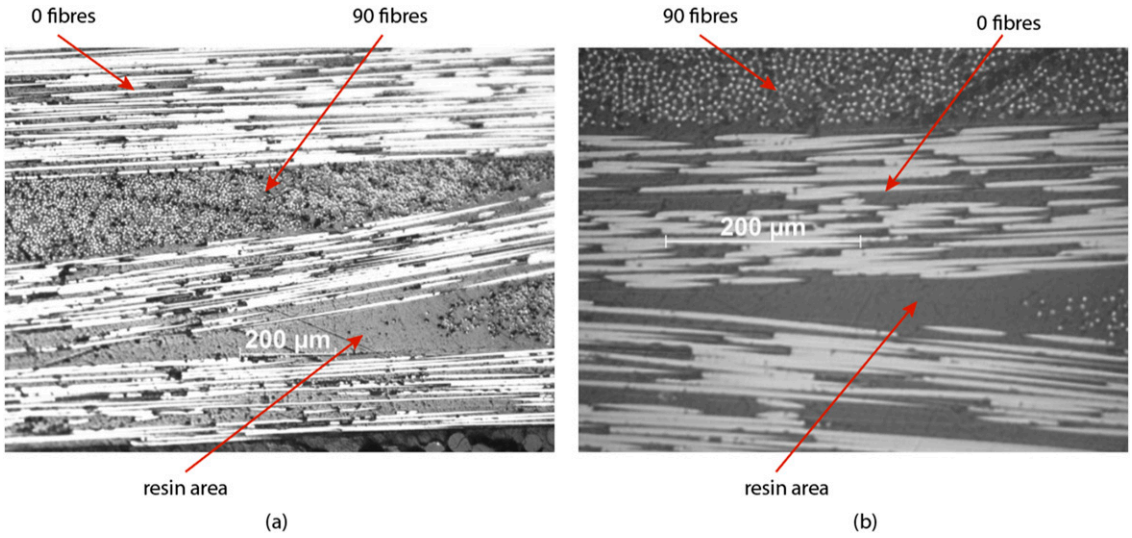

Figure 12. Embedded samples under optical microscopy at magnifications of (a) 10× and (b) 20×.

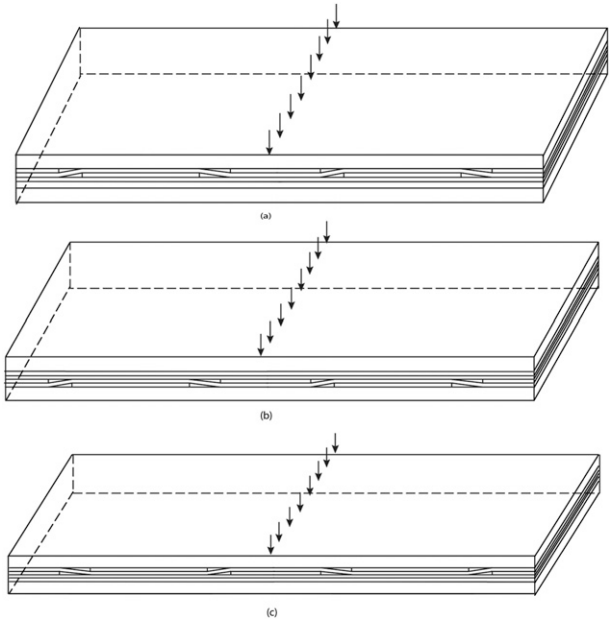

Figure 13. Structure of specimens: (a) structure A, (b) structure B, and (c) structure C.

Test 3 in Table 3 and test 8 in Table 5 indicate that the fibers in the top five layers broke when using a loading nose with a 15mm diameter. This suggests that smaller loading nose radii result in higher stress concentrations in the loading area. In test 4, the 25mm diameter loading nose penetrated the silicone pad, causing the fibers in the top layers to break.

The results of test 4 with structure A closely resemble those of test 5 with structure B, as shown in Table 4. A comparison between the results of tests 5 and 7 demonstrates that the silicone pads absorbed a certain amount of energy, leading to a higher damage initiation load when thicker silicone pads were used. Additionally, the initiation load for the same nominal structure, but using one silicone pad versus two silicone pads, was 59N/mm.

A comparison between tests 8 and 9 indicates that the size of the loading nose had an impact on the damage initiation load and location. A smaller loading nose resulted in a higher stress concentration in the loading area. In test 8, the stress concentration was higher than in test 9, causing the fibers in the top layers to fail when the maximum stress was reached. On the other hand, in test 9, the tension stress in the bottom layers was equal to or higher than the tension failure strength of the fibers, leading to their failure.

Comparing tests 7 and 9 shows a difference of approximately 4.5% in terms of initiation load. It is difficult to qualitatively determine the effect of the loading nose size on the damage initiation load by comparing tests 8 and 9. When using a 25mm loading nose and two silicone pads, the fibers on the bottom surface were broken through tension only. Stress concentration in the loading area and the fibers reached the maximum compression load, resulting in the breaking of fibers on the top surface in tests 3, 4, 5, and 8. It is important to note that there were not enough tests of the same type to statistically evaluate the significance of the loading nose size and tab thickness. Additionally, differences in failure mode may fall within the experimental scatter. Therefore, the discussion presented here mainly aims to identify trends.

Tests were conducted on specimens with configurations A, B, and C using a 25mm loading nose and either one or two silicone pads. Table 5 reveals that the fibers in configuration C failed earlier compared to configurations A and B, even when an additional silicone pad was used and thus resulted in a higher damage

initiation load. The difference of specimen with configuration C from those with configurations A and B suggests that the geometry of the specimen may be a contributing factor but there were not enough specimens to quantify this difference.

The size of the loading nose and the number of silicone pads used in the test influenced the damage initiation load and location. A smaller loading nose and fewer silicone pads led to damage initiation in the top layer. The structure failed shortly after the fibers in the top five layers failed, resulting in induced delamination in tests 4 and 6. The location of the broken fibers clearly demonstrated the impact of the loading nose size and number of silicone pads used.

It can be observed from Table 4 that in the case of structure B, the initiation load for test 7 using 2 silicone pads is higher than that of test 5 using only 1 silicone pad. This observation is logical since silicone pads are soft, and the greater the number of silicone pads, the more energy they can absorb. However, tests 5 and 6 in Table 5 exhibit a contrasting trend. Based on the damage depicted in Figure 14, it is inferred that manufacturing defects in the specimen of test 5 may have led to a different damage mode compared to test 6, affecting both the damage pattern and the initiation load.

In test 5, there were two areas where fibers broke, and these areas were subsequently connected by delamination, as shown in Figure 14. The distance between the two locations was smaller than the loading nose diameter. Additionally, delamination, due to shear stress, occurred at the interface of two layers, not following the pattern of broken fibers. Microscopy images were taken to examine delamination near the resin areas in test 5, as shown in Figure 15. The propagation path of the delamination at the interface followed the woven ply.

The captured images in test 5, as depicted in Figure 16, have successfully shown the initiation of delamination from the resin area (shown in Figure 16(c), the red part) after the fibers were broken. The areas of damage, marked in red circles, indicate the presence of broken fibers and visible delamination on the left side. Figure 16(b) was taken 1 s after Figure 16(a), providing a sequential view of the damage progression.

The main focus of the test program was to examine the delamination that originated from the resin pocket. However, the occurrence of matrix cracking in other tests was an unintended by-product resulting from the sensitivity of the specimens to slight variations in loading and geometry. It is important to note that this research did not specifically address the modeling of matrix cracks.

Figure 17 displays the damaged specimens from tests 7 and 9. Unlike tests that were terminated immediately after the sound of initial damage, tests 7 and 9 continued until structural failure, even after the fibers were broken. The failure of the matrix in the 90 plies was attributed to transverse shear stress, with cracking occurring at a 45° angle. The propagation of delamination was primarily

Table 3. Test results of specimens with structure A.

	Diameter of loading nose	Number of silicone pads	Initiation load	Damage location
Test 3	15mm	0	115.2 N/mm	Top
Test 4	25mm	1	151.1 N/mm	Top

Table 4. Test results of specimens with structure B.

	Diameter of loading nose	Number of silicone pads	Initiation load	Damage location
Test 5	25mm	1	148.99 N/mm	Top
Test 7	25mm	2	208.40 N/mm	Bottom
Test 8	15mm	2	164.49 N/mm	Top
Test 9	25mm	2	198.78 N/mm	Bottom

Table 5. Test results of structures A, B, and C (from top to bottom).

	Diameter of loading nose	Number of silicone pads	Initiation load	Damage location
Test 4	25mm	1	151.123 N/mm	Top
Test 5	25mm	1	148.99 N/mm	Top
Test 6	25mm	2	139.58 N/mm	Top

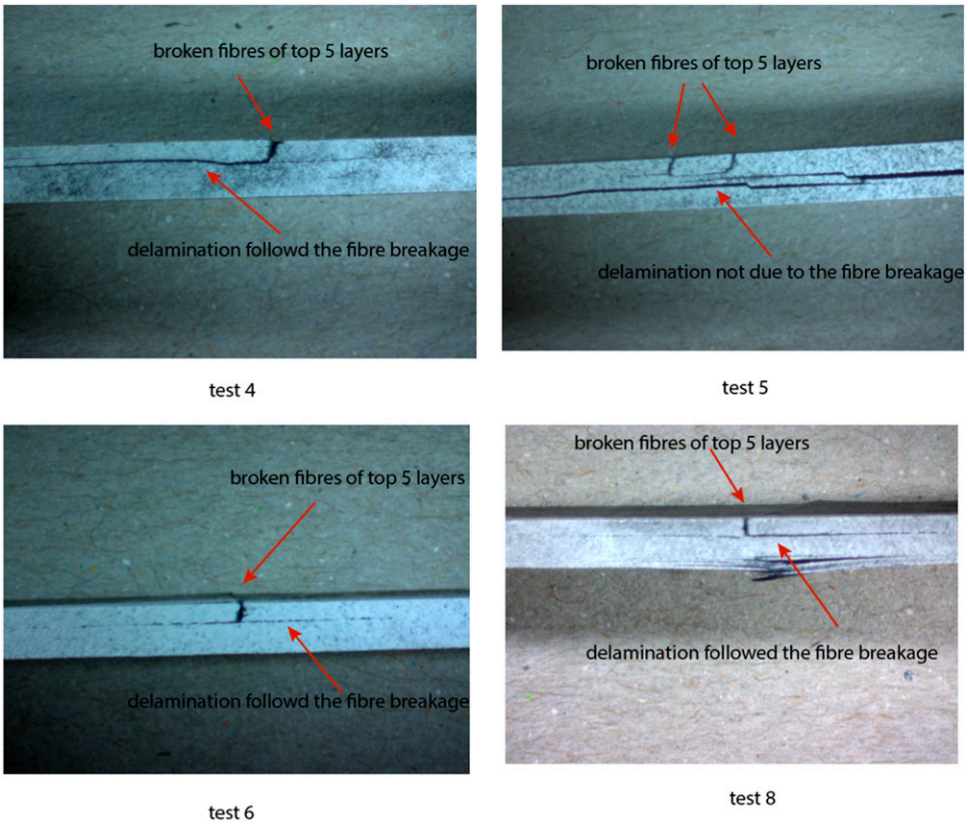

Figure 14. Damage of specimen tests.

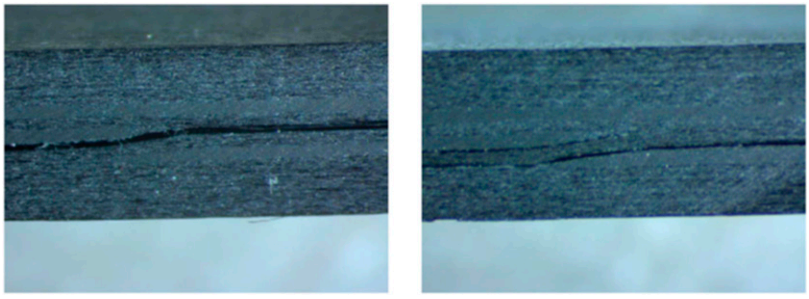

Figure 15. Delamination in the resin area in test 5.

driven by matrix failure in the 90° plies, as concluded from test 7.

Comparisons with simulations

Cohesive zone model. Multiple finite element models were developed to simulate the tests conducted in this study. A 24-layer finite element model was created to simulate transverse matrix failure in the bottom layers and the subsequent delamination. Under three-point bending, failure is shear dominated so mode I contribution was neglected and no mode mixity was used. Cohesive elements with a thickness of 0.001mm were introduced in the middle of the specimen at the bottom and on the interface between the bottom 0_5 and 90_5 layers, which were under the loading point. The length of each cohesive element was 0.005mm. For the cohesive elements, the bilinear traction-separation law was implemented in ABAQUS using COH2D4 elements. The shape of the law can be defined by the penalty stiffness $\mathrm{K} = 6 \times 10^7 N/mm^3$ and the interfacial strengths $t_n = t_s = t_t = 66.2MPa$. In the simulation model, the element will fail when the damage equal to 0.99 in the element. Damage evolution was controlled by the energy of the interface. The critical energy release rate $K_c = 1.58KJ/m^2$.

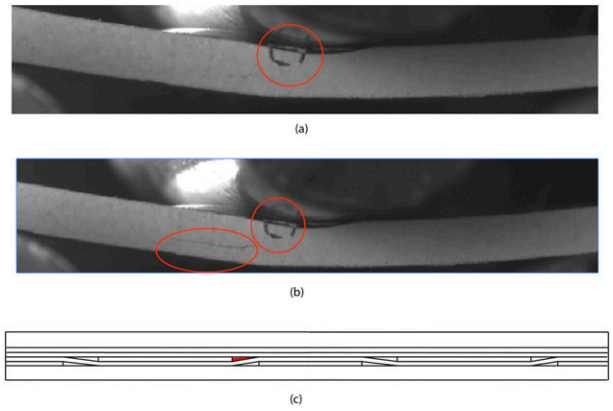

Figure 16. Delamination initiation in test 5.

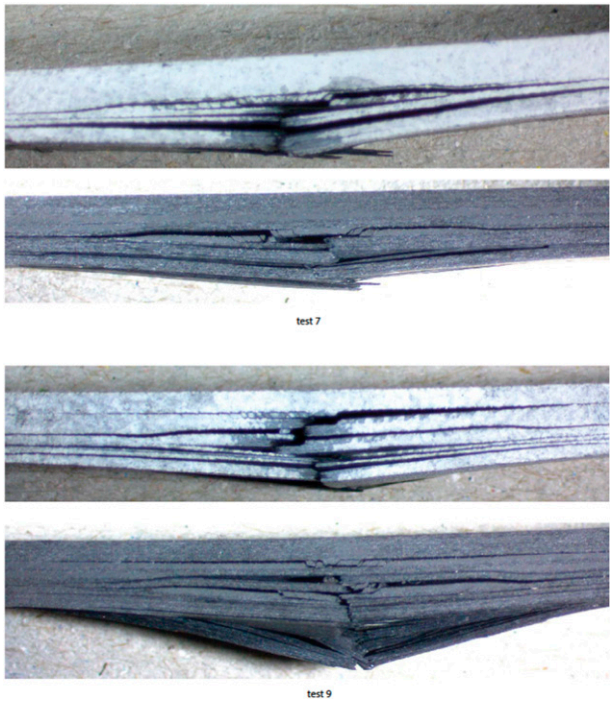

Figure 17. Tests in which damage initiated from bottom layers.

There were approximately 19,000 cohesive elements in the models. The size of the cohesive elements in the cohesive layers was kept the same in all models. The remaining elements used in the model were 2D continuum solid quadrilateral elements CPS4R, and few CPS3 triangular elements. There were 612,800 CPS4R elements and 6130 CPS3 elements. These resulted in approximately 5,091,500 degrees of freedom. The mesh of the model could be seen in Figure 18. The material properties for the resin are at the beginning of subsection and the ply in Table 1. The location of the cohesive elements in the models is designed according the specific test. The cohesive elements are in the middle of y direction in the finite element model for test 1 and test 2, and the cohesive elements are close to the resin area in the model for test 5, as can be seen in Figure 18.

Comparisons. The predicted initiation load for transverse matrix failure was 60N, and in tests 1 and 2, the initiation loads acting on the matrix were 47.93N and 49.435N, respectively, at the same location. It should be noted that the predicted failure load was higher than the actual test failure load due to the assumption of defect-free specimens. Additionally, the limited number of test results may affect the statistical significance of the predicted values.

In the specific test shown in Figure 16, the delamination length a was 1 mm when the applied load was 149N/mm. In the finite element simulation, when the delamination of the same size occurred at the same location, the predicted load was 121.04N/mm. This indicates that the predicted damage initiation load was approximately 19% lower than the actual test load. The discrepancy can be partly attributed to inaccuracies in the test method and the approximation of the geometry of the woven ply.

For the 14-layer specimens, two important considerations should be noted in the finite element modeling: (1) the large deformations experienced by the specimens when the fibers break were not accounted for in the simulation, and (2) the failure analysis of fibers requires more representative cohesive elements. Although nonlinear geometry analysis is not inherently problematic, the combination of nonlinear deformation and cohesive elements can result in long simulation times and convergence issues. In this study,

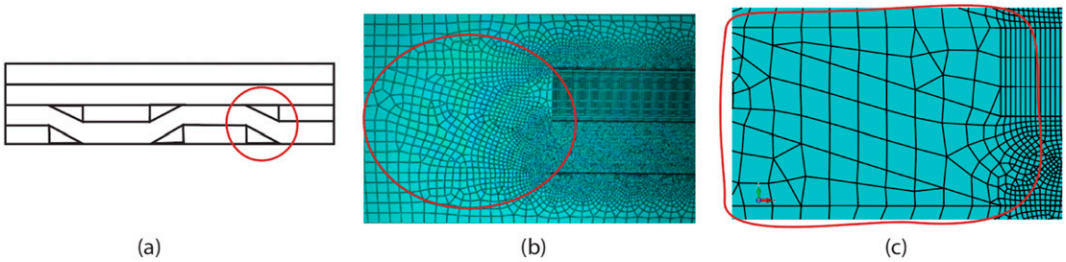

Figure 18. Mesh in the finite element model for test 5.

the focus was primarily on the onset and growth of delamination in AP-PLY patterns. Conducting a linear analysis initially, which isolates the parameters of interest, is deemed beneficial. Nonlinear effects, which are undesirable at this stage, can be avoided by modifying the specimen geometry, such as using a thicker specimen or adjusting the spacing of loading tabs. The transverse tensile strength could be used to define damage initiation, but the parameter for transverse tensile fracture energy in the damage evolution definition remains unknown. Further improvements can be made in modeling the failure of the specimens. In future work, it would be worth investigating the use of user-defined cohesive elements when analyzing broken fibers, provided that the associated traction-separation law is known.

Conclusions

A series of tests were conducted to study delamination initiation and propagation in a woven AP-PLY composite beam subjected to an out-of-plane load. The initial two tests indicated that specimens with a 90-layer outer region failed early due to transverse matrix cracking and compression failure under the loading tabs. Consequently, the outer 90 layers were removed from the remaining specimens. Various test setups were employed to investigate the most effective method of identifying the onset and growth of failure among different configurations. These tests serve as preliminary trials aiming to identify the configuration that triggers delamination at the resin pocket of the AP-PLY pattern.

Two parameters, namely the size of the loading nose and the number of silicone pads used between the loading nose and specimen, were considered in the tests as they affect the load where damage initiation occurs and the location of the damage initiation. The use of a 15 mm diameter loading nose resulted in fiber breakage on the top surface even when two silicone pads with 1.08 mm thickness in total were used between the loading tab and the specimen. On the other hand, the use of a 25 mm diameter loading nose and one silicone pad led to fiber breakage in the top layers. The silicone pads absorbed a certain amount of load energy, thereby increasing the damage initiation load in tests with more silicone pads compared to tests with fewer pads. Additionally, a larger loading nose resulted in a higher damage initiation load. The critical load for fiber breakage under tension in the three-point bending test was determined for a specific geometry and test setup.

The predicted damage initiation load exhibited an approximate 20% deviation from the actual test load. This discrepancy stems from five key factors: (1) disparities between the geometry of the loading nose and rods utilized in the tests, compared to the supporting boundary conditions and loading conditions employed in the simulation; (2) the absorption of a portion of the loading energy by the silicone pads during testing; (3) an erroneous assumption in the simulation model that it is free from defects, whilst this is not the case in reality; (4) the limitations of the particular cohesive element in fully replicating the intricate damage resulting from delaminations and fiber breakage observed in the test; and (5) slight discrepancies between the microstructure of the AP-PLY model and the actual test specimen.

In the tests, the damage observed was a combination of transverse matrix failure, delamination induced by fiber breakage and delamination caused by transverse shear stresses. It was difficult to distinguish the mode II delamination from all other forms of damage. In one of the tests, the desired failure mode, namely a delamination following the woven path of the AP-PLY pattern was observed but it occurred simultaneously with the fiber failure. It is necessary to perform more tests to determine the delamination behavior of an AP-PLY composite beam in a three-point bending test.

Declaration of conflicting interests

The author(s) declared no potential conflicts of interest with respect to the research, authorship, and/or publication of this article.

Funding

The author(s) disclosed receipt of the following financial support for the research, authorship, and/or publication of this article: This work has been supported by the Natural Science Basic Research Program of Shaanxi (Grant No. D5110230104).

ORCID iD

Weiling Zheng https://orcid.org/0000-0001-6211-4829

Data availability statement

Data will be made available on request.

References

1. Tsai S and Wu E. A general theory of strength for anisotropic materials. *J Compos Mater* 1971; 5(1): 58–80.
2. Hashin Z. Failure criteria for unidirectional fiber composites. *J Appl Mech* 1980; 47(2): 329–334.
3. Christensen R. Stress based yield/failure criteria for fiber composites. *Int J Solid Struct* 1997; 34(5): 529–543.
4. Puck A and Schürmann H. Failure analysis of frp laminates by means of physically based phenomenological models. *Compos Sci Technol* 1998; 58(7): 1045–1067.
5. Saghizadeh H and Dharan C. Delamination fracture toughness of graphite and aramid epoxy composites. *J Eng Mater Technol* 1986; 108(4): 290–295.
6. Benzeggagh M and Kenane M. Measurement of mixed-mode delamination fracture toughness of unidirectional glass/epoxy composites with mixed-mode bending apparatus. *Compos Sci Technol* 1996; 56(4): 439–449.
7. Kim B and Mayer A. Influence of fiber direction and mixed-mode ratio on delamination fracture toughness of carbon/epoxy laminates. *Compos Sci Technol* 2003; 63(5): 695–713.
8. Oskouei AR, Zucchelli A, Ahmadi M, et al. An integrated approach based on acoustic emission and mechanical

information to evaluate the delamination fracture toughness at mode i in composite laminate. *Mater Des* 2011; 32(3): 1444–1455.
9. Nag´elsmit MH, Kassapoglou C and Gürdal Z. AP-PLY a new fiber placement architecture for fabric replacement. *SAMPE J* 2011; 47(2): 36–45.
10. Nagelsmit MH. *Fibre placement architectures for improved damage tolerance*. Delft: TU Delft, 2013.
11. Whitney T and Chou T. Modeling of 3d angle-interlock textile structural composite. *J Compos Mater* 1989; 23(9): 890–911.
12. Ishikawa T and Chou T. Stiffness and strength behavior of woven fabric composites. *J Mater Sci* 1982; 17(11): 3211–3220.
13. Naik N and Kuchibhotla R. Analytical study of strength and failure behaviour of plain weave fabric composites made of twisted yarns. *Compos Part A Appl Sci Manuf* 2002; 33(5): 697–708.
14. Sankar B and Marrey R. Analytical method for micromechanics of textile composites. *Compos Sci Technol* 1997; 57(6): 703–713.
15. Woo K and Whitcomb J. Three-dimensional failure analysis of plain weave textile composites using a global/local finite element method. *J Compos Mater* 1996; 30(9): 984–1003.
16. Tan P, Tong L and Steven GP. Modeling approaches for 3d orthogonal woven composites. *J Reinf Plast Compos* 1998; 17(6): 545–577.
17. Chen L, Tao X and Choy C. Mechanical analysis of 3-d braided composites by the finite multiphase element method. *Compos Sci Technol* 1999; 59(16): 2383–2391.
18. Byun J and Chou T. Elastic properties of three-dimensional angle-interlock fabric preforms. *J Text I* 1990; 81(4): 538–548.
19. Madenci E, Ozkilic Y and Gemi L. Buckling and free vibration analyses of pultruded GFRP laminated composites: experimental, numerical and analytical investigations. *Compos Struct* 2020; 254: 112806.
20. Zhao Y, Song L, Li J, et al. Multi-scale finite element analyses of thermal conductivities of three dimensional woven composites. *Appl Compos Mater* 2017; 24(6): 1525–1542.
21. Gemi L, Kayrich M, Uludag M, et al. Experimental and statistical analysis of low velocity impact response of filament wound composite pipes. *Compos Part B-Eng* 2018; 149: 38–48.
22. Cai D, Tang J, Zhou G, et al. Failure analysis of plain woven glass/epoxy laminates: comparison of off-axis and biaxial tension loadings. *Polym Test* 2017; 60: 307–320.
23. Zheng W and Kassapoglou C. Prediction of delamination onset and growth for ap-ply composite laminates using the finite element method. *Compos Part A Appl Sci Manuf* 2017; 101: 381–393.
24. Zheng W and Kassapoglou C. Energy method for the calculation of the energy release rate of delamination in composite beams. *J Compos Mater* 2019; 53(4): 425–443.
25. Zheng W, Kassapoglou C and Zheng L. Tailoring of ap-ply composite laminates for improved performance in the presence of delaminations. *Compos Struct* 2019; 211: 89–99.
26. Li X, Dufty J and Pearce G. Automation of tow wise modelling for automated fibre placement and filament wound composites. *Compos Part A Appl Sci Manuf* 2021; 147: 106449.
27. Li X, Brown S, Joosten M, et al. Tow wise modelling of non-conventional automated fibre placement composites: short beam shear study. *Compos Part A Appl Sci Manuf* 2022; 154: 106767.